

Measurement of the reaction $\gamma p \rightarrow K^0 \Sigma^+$ at photon energies up to 2.6 GeV^{*}

R. Lawall^{1,a}, J. Barth¹, C. Bennhold³, K.-H. Glander¹, S. Goers¹, J. Hannappel¹, N. Jöpen¹, F. Klein^{1,b}, E. Klempt², T. Mart⁴, D. Menze¹, M. Ostrick¹, E. Paul¹, I. Schulday¹, W.J. Schuille¹, F.W. Wieland¹, C. Wu¹

¹ Physikalisches Institut der Universität Bonn, Germany

² Helmholtz-Institut für Strahlen- und Kernphysik Bonn, Germany

³ Dep. of Physics, George Washington University, Washington DC, USA

⁴ Departemen Fisika, FMIPA, Universitas Indonesia, Depok 16424, Indonesia

Received: date / Revised version: date

Abstract. The reaction $\gamma p \rightarrow K^0 \Sigma^+$ was measured in the photon energy range from threshold up to 2.6 GeV with the SAPHIR detector at the electron stretcher facility, ELSA, in Bonn. Results are presented on the reaction cross section and the polarization of the Σ^+ as a function of the kaon production angle in the centre-of-mass system, $\cos \Theta_K^{c.m.}$, and the photon energy. The cross section is lower and varies less with photon energy and kaon production angle than that of $\gamma p \rightarrow K^+ \Sigma^0$. The Σ^+ is polarized predominantly at $\cos \Theta_K^{c.m.} \approx 0$. The data presented here are more precise than previous ones obtained with SAPHIR and extend the photon energy range to higher values. They are compared to isobar model calculations.

PACS. PACS-key describing text of that key – PACS-key describing text of that key

1 Introduction

Hadronic final states produced in hadron- or photon-induced reactions on nucleons at low energies are investigated with respect to production mechanisms, in particular to the formation of baryonic resonances which decay into hadrons. Most of the known nucleon and delta resonances were discovered in this way. However, model calculations ([1], [2]) predict more resonant states than have been observed in experiments so far. Some of the missing non-strange resonances are predicted to decay into final states comprising strange particle pairs.

The SAPHIR experiment has measured such final states. Results on the reactions $\gamma p \rightarrow K^+ \Lambda$ and $\gamma p \rightarrow K^+ \Sigma^0$ were published elsewhere [3]. Here we report about the reaction $\gamma p \rightarrow K^0 \Sigma^+$ which adds another isospin configuration of the $K \Sigma$ final state.

Results on $\gamma p \rightarrow K^0 \Sigma^+$ based on 30 million triggers from earlier data taking with SAPHIR were published [4]. The new results presented here are based on 180 million triggers which were taken with an upgraded SAPHIR detector setup in an extended photon energy range from reaction threshold up to 2.6 GeV. This measurement of cross

sections is more reliable than the previous one, since it has been found that, in the previous analysis, background from other reactions was underestimated and not sufficiently eliminated from the event sample of the reaction $\gamma p \rightarrow K^0 \Sigma^+$. In the current analysis this background has been removed thoroughly. The new cross sections show systematically lower values.

The data are available via internet.¹

2 The experiment

Data were taken with the magnetic multiparticle spectrometer SAPHIR [5] at the 3.5 GeV electron stretcher facility ELSA [6]. The setup is shown schematically in fig. 1. An extracted electron beam of 2.8 GeV was directed on a radiator target to provide an energy-tagged photon beam within the range from 0.868 to 2.650 GeV. The data taking was based on a trigger defined by a coincidence of signals from the scattered electrons in the tagging system with at least two charged particles in the scintillator hodoscopes and no signal from a beam-veto-counter downstream of SAPHIR which detected non-interacting photons.

The drift chambers served to measure charged particles. The scintillator hodoscopes were used for time-of-flight (TOF) measurements which allowed together with the track momentum (measured with the drift chambers in

^{*} This work is supported in part by the Deutsche Forschungsgemeinschaft (DFG) (SPP KL 980/2-3)

^a Part of doctoral thesis (R.Lawall, doctoral thesis, Bonn University (2004), Bonn-IR-2004-01), <http://saphir.physik.uni-bonn.de/saphir/thesis.html>

^b email: klein@physik.uni-bonn.de

¹ <http://saphir.physik.uni-bonn.de/saphir/publications>

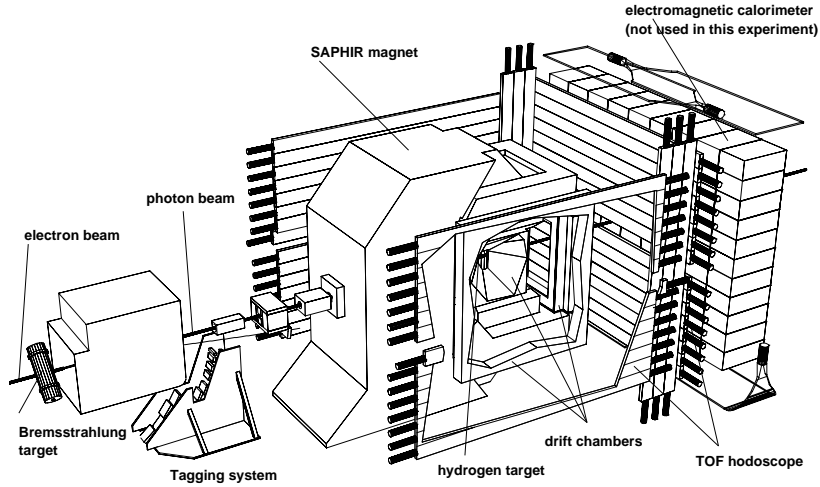


Fig. 1. Sketch of the SAPHIR detector.

M. Bockhorst & J. Link

the magnetic field) to calculate the particle masses. The experimental set-up of SAPHIR was upgraded for this data taking. A new tagging system [7] with improved energy resolution and extended electron energy range was installed. A planar drift chamber was added to the central drift chamber which improved the track reconstruction in forward direction [8]. The data analyzed here stem from four data taking periods in 1997 and 1998.

3 Event reconstruction and event selection

The events of the reaction $\gamma p \rightarrow K^0 \Sigma^+$ were reconstructed from the measurement of the charged decay products from $K_S^0 \rightarrow \pi^+ \pi^-$, $\Sigma^+ \rightarrow p \pi^0$ and $\Sigma^+ \rightarrow n \pi^+$ respectively (see fig. 2). The measured 3-momenta of the positively and negatively charged particles together with the incident photon energy (measured in the tagging system) provided all the information needed to reconstruct the complete event topology and to determine the 3-momenta of the unmeasured particles, i.e. Σ^+ , K_S^0 and the neutral decay particle π^0 or n , respectively, by kinematical fits.

First the unmeasured K_S^0 decay was reconstructed by extrapolating two tracks of opposite charge back to the decay vertex. Using the energy measurement of the incident photon and the reconstructed 3-momentum of the K_S^0 candidate a kinematical fit was carried out assuming the primary reaction $\gamma p \rightarrow K_S^0 \Sigma^+$ which yielded the momentum of the missing Σ^+ .

In the next step the primary vertex and the Σ^+ decay were reconstructed simultaneously by an iterative method that was already described in a previous publication [4]. The positively charged track (not belonging to the K_S^0 candidate) and the Σ^+ track at the Σ^+ decay vertex allowed to reconstruct the four-momentum of the neutral decay particle n or π^0 , respectively.

An event was accepted if it was successfully fitted to the kinematics of the complete reaction while the assigned

charged particle masses were consistent with the TOF-measurements or undetermined (for tracks which were outside the geometrical acceptance of the hodoscopes or had no signal due to hodoscope inefficiencies).

The reconstructed decay time distributions of K_S^0 and Σ^+ are shown in figs. 3 and 4 respectively. Monte-Carlo simulated events assuming the proper K_S^0 lifetime are also drawn. The comparison indicates that there is a substantial excess of background from other reactions mainly at low decay times for K_S^0 and at a smaller scale at large decay times for Σ^+ . In order to reduce this background the event sample was restricted to $\tau_{K_S^0} > 0.7 \cdot 10^{-10} s$ and $\tau_{\Sigma^+} < 5 \cdot 10^{-10} s$.

These cuts were not sufficient to remove the falsely included events completely. In particular, the main back-

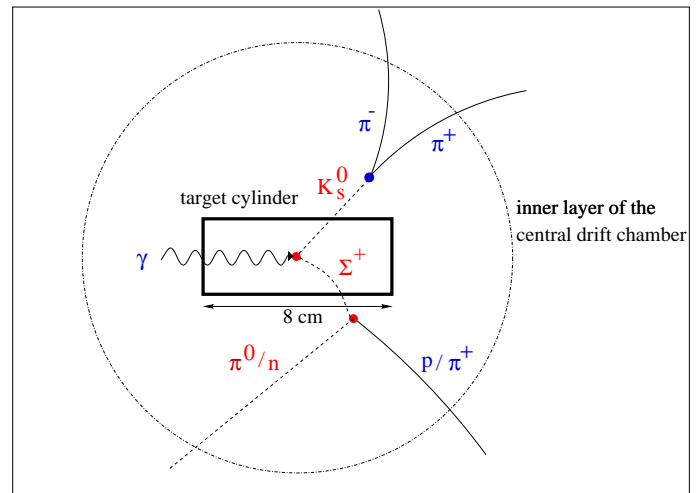


Fig. 2. Event topology of $\gamma p \rightarrow K_S^0 \Sigma^+$ with the decays $K_S^0 \rightarrow \pi^+ \pi^-$ and $\Sigma^+ \rightarrow p \pi^0 / n \pi^+$. The full lines indicate the measured tracks of charged particles. The dashed lines indicate the unmeasured particle tracks of K_S^0 , Σ^+ and n or π^0 , respectively.

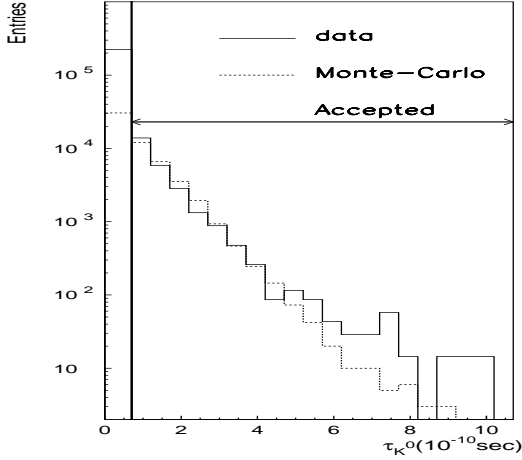


Fig. 3. Decay time distribution of K_S^0 for data (full line) and for Monte-Carlo simulated events (dashed line). The vertical line indicates the cut applied.

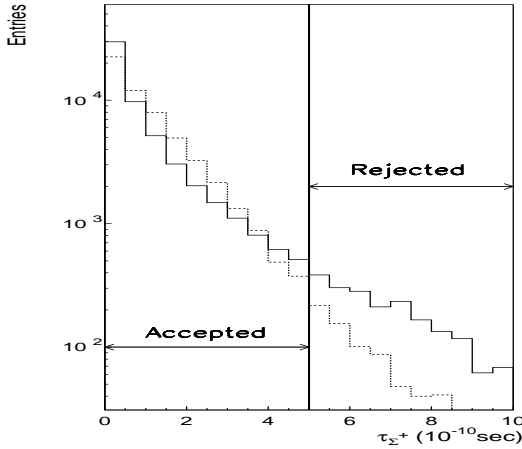


Fig. 4. Decay time distribution of Σ^+ candidates for data (full line) and for Monte-Carlo simulated events (dashed line). The vertical line indicates the cut applied.

ground reactions $\gamma p \rightarrow p\pi^+\pi^-\pi^0$ and $n\pi^+\pi^+\pi^-$ were still present in the accepted ranges of the decay times of K_S^0 and Σ^+ according to the limited spatial resolution of the decay vertices.

Since such background events must have a common vertex formed by three charged tracks, corresponding background reactions were simulated (see sect. 5) and studied with respect to the probability of the vertex fit. The dependence of the reaction cross section from a cut on this probability after all other selection cuts is displayed in fig. 5 (total distribution). The light grey area represents the estimated total background from other reactions (see table 1 in sect. 5). Events with a vertex fit probability bigger than 10^{-3} were removed both in data and simulated background events. The cut was chosen so that the background contribution to the cross section was at most about 10% on average. The final cross section (dark grey area) was

obtained by subtraction of the accumulated background events (see sect. 6).

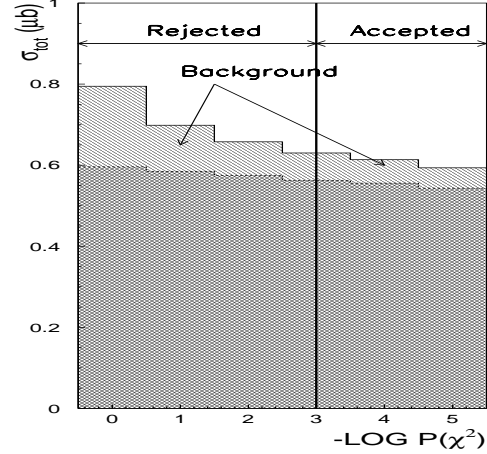


Fig. 5. The directly measured reaction cross section and the background subtracted cross section (dark grey area) as a function of the cut on the primary vertex probability. The light grey area represents the background contribution (see text). The vertical line indicates the cut applied.

The following plots display the final data sample after all cuts: fig. 6 depicts the invariant mass distribution of the $\pi^+\pi^-$ system at the kaon decay vertex corresponding to the K_S^0 mass, and the missing mass distribution calculated at the primary vertex, corresponding to the unmeasured Σ^+ signal. In fig. 7 the squared missing mass distributions at the Σ^+ decay vertex are shown, corresponding to π^0 and n , respectively. The missing mass at the primary vertex was calculated from the 4-momenta of the incident γ and the reconstructed K_S^0 assuming the reaction $\gamma p \rightarrow K_S^0 \Sigma^+$. The missing mass squared at the Σ^+ decay vertex was calculated from the 4-momenta of Σ^+ and p/π^+ , respectively.

4 Acceptance of the events

The acceptance was determined by means of Monte-Carlo simulations. Events of the reaction $\gamma p \rightarrow K_S^0 \Sigma^+$ were generated according to phase space with propagation of both particles according to their lifetimes and the decays $K_S^0 \rightarrow \pi^+\pi^-$ and $\Sigma^+ \rightarrow p\pi^0/n\pi^+$. Charged particles in the final state were tracked through the drift chamber system of the SAPHIR detector taking into account the magnetic field and multiple scattering in all materials of the detector setup passed by the particles. Simulated events were treated like real events. The determination of the acceptance comprised the trigger efficiency of the data taking periods, the event reconstruction efficiency and the data reduction according to the event selection cuts. The acceptance was 3.4% on average varying between 2 and 8% throughout the kinematical range spanned by the com-

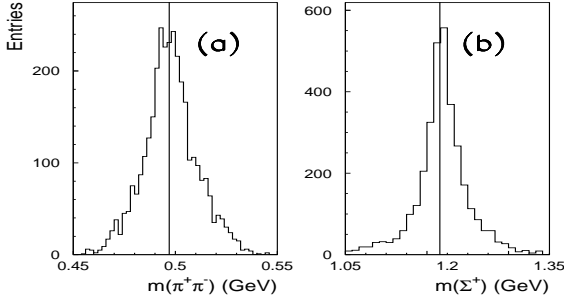


Fig. 6. (a): Distribution of the invariant mass of the $\pi^+\pi^-$ system; (b): Distribution of the missing mass calculated at the primary vertex (see text).

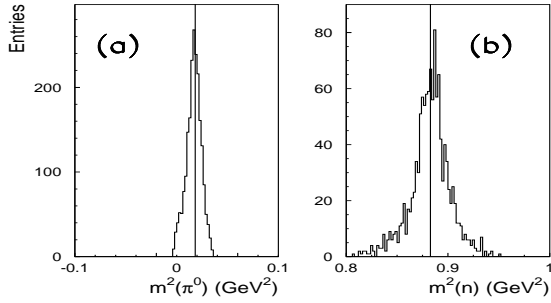


Fig. 7. Distribution of the missing mass squared for (a) $\Sigma^+ \rightarrow p\pi^0$, (b) for $\Sigma^+ \rightarrow n\pi^+$ (see text).

plete K_S^0 production angular range in the CMS and the photon energy range of the data.

5 Background from other reactions

In order to estimate possible background contributions the reactions listed in table 1 were simulated according to phase space assuming a $1/E_\gamma$ dependence in the photon energy range of the data and processed like real data through the reconstruction and selection procedure.

The acceptance of background of events falsely selected as $\gamma p \rightarrow K_S^0 \Sigma^+$ and the estimates of their contributions in terms of cross sections obtained on average after all cuts are shown in Table 1. The errors of the cross sections (last column) are in the order of 10% or less.

The background contributions were also quantified in bins of the photon energy and the K_S^0 production angle. The reactions $\gamma p \rightarrow p\pi^+\pi^-\pi^0$ and $\gamma p \rightarrow n\pi^+\pi^+\pi^-$ contribute preferentially at low energy and in backward direction in the center of mass system. To give an example, fig. 8 shows simulated events of $\gamma p \rightarrow p\pi^+\pi^-\pi^0$ which were falsely accepted as events from the reaction $\gamma p \rightarrow K^0 \Sigma^+$ in the analysis procedure, distributed in the $E_\gamma - \cos \Theta_K^{c.m.}$ plane. The numbers of events were weighted by multiplying with E_γ to enhance the rare events at high E_γ . Smaller, but non-negligible contributions stem from the

reactions $\gamma p \rightarrow K\Lambda\pi$ which contribute preferentially at higher energies and towards higher K_S^0 production angles (not shown).

For subtracting the background as a function of the photon energy and the K_S^0 production angle the sum of the contributions of all the reactions was taken into account bin-by-bin (see sect. 6).

Table 1. Considered reactions, their cross sections throughout the photon energy range, calculated acceptances of events falsely selected as reaction $\gamma p \rightarrow K^0 \Sigma^+$ (A), and effective cross sections with which they contribute to $\gamma p \rightarrow K^0 \Sigma^+$ (last column). The last row gives the accumulated contributions of all background channels together.

Reaction	σ (μb)	A (10^{-2})	$\frac{A}{A_{K\Sigma}} \cdot \sigma$ (μb)
$p\pi^+\pi^-$	20 - 55	0.0002	0.0032
$p\pi^+\pi^-\pi^0$	6 - 28	0.0062	0.0503
$n\pi^+\pi^+\pi^-$	3 - 10	0.0031	0.0090
$K^+\Lambda\pi^0$	0.5	0.0100	0.0014
$K_S^0\Lambda\pi^+$	0.5	0.0110	0.0016
$K_L^0\Lambda\pi^+$	0.5	0.0100	0.0014
$K_S^0\Sigma^+\pi^0$	0.2	0.0060	0.0003
$K^+\Lambda$	1.0	0.0030	0.0009
$K^+\Sigma^0$	1.0	0.0010	0.0003
Total			0.0684

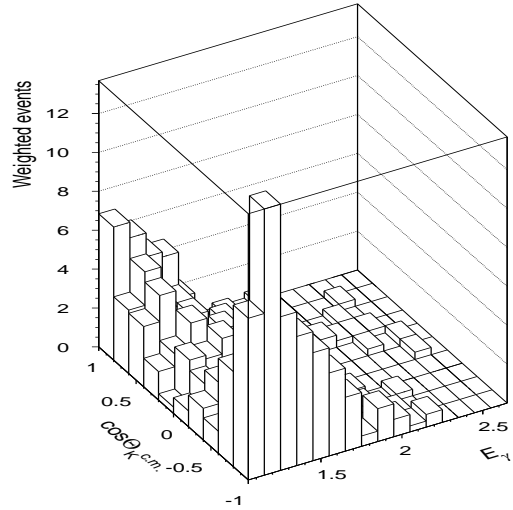


Fig. 8. Distribution of simulated $p\pi^+\pi^-\pi^0$ events as a function of the photon energy and the K^0 production angle, falsely identified as $\gamma p \rightarrow K^0 \Sigma^+$.

6 Results

The final event sample of the reaction consisted of 3310 events, 2114 with the decay $\Sigma^+ \rightarrow p\pi^0$ and 1196 with the decay $\Sigma^+ \rightarrow n\pi^+$. For each data taking period, cross sections were determined in bins of the photon energy, E_γ , and of the K^0 production angle in the γp center-of-mass system, $\cos\Theta_K^{c.m.}$. They were calculated separately for both Σ^+ decay modes taking into account the branching ratios. The cross sections obtained were found to be consistent with each other.

Background contributions to the cross sections stemming from other reactions (see sect. 5) were also determined separately for each data taking period using the same binning. The errors were calculated by quadratic addition of the statistical errors and the assumed normalization uncertainty of 10% (see sect. 5). Fig. 9 shows as an example the distributions of the measured cross section of $\gamma p \rightarrow K^0 \Sigma^+$ corrected for the branching ratios of K_S^0 and Σ^+ decays and the estimated background from $\gamma p \rightarrow p\pi^+\pi^-\pi^0$ and $n\pi^+\pi^+\pi^-$ in the photon energy range between 1.150 and 1.250 GeV.

The accumulated background contributions were subtracted bin-by-bin separately for each data taking period. The errors of the subtracted cross sections were calculated by quadratic addition of the single errors. Finally, the cross sections were calculated as statistically weighted

means of the subtracted cross sections of the four data taking periods. Two sorts of errors were calculated: at first the statistical error of the weighted mean of the four measurements, σ_w , and secondly the standard deviation of the four measurements from the weighted mean, σ_d . In case $\sigma_d > \sigma_w$ it was assumed that the error σ_d accounts for systematic uncertainties in the run conditions which were not properly taken into account in the simulation. The larger of the two errors was accepted as total error. A more detailed discussion of the error calculation can be found in [8], [9].

Differential cross sections after subtraction are shown in fig.10. The corresponding values are given in table 2.

The reaction cross sections as a function of the photon energy were obtained by summing up the differential cross sections over the angular range. Errors were determined by quadratic addition of the single errors in the angular bins. The results are shown in fig. 11 and table 3. Previous measurements [4], [10] are also shown.

The cross sections from the previous data set taken at SAPHIR [4] are 30 to 40% higher than the current results. Careful investigations carried out in the course of the new analysis have shown that background, in particular from $\gamma p \rightarrow p\pi^+\pi^-\pi^0$, had not been removed sufficiently in the analysis of the first data set and moreover the error calculations did not account sufficiently for this uncertainty. The polarization of the Σ^+ -hyperon has been measured through its parity-violating weak decay. The angular distribution of the decay nucleon is given by [11]:

$$W(\theta_N) = \frac{1}{2} \cdot (1 + \alpha \cdot P \cdot \cos(\theta_N))$$

where α is the asymmetry parameter which is equal to $(-0.98^{+0.017}_{-0.015})$ for $\Sigma^+ \rightarrow p\pi^0$ and $(0.068^{+0.013}_{-0.013})$ for $\Sigma^+ \rightarrow n\pi^+$ [12]. The parameter P measures the hyperon polarization and θ_N is the decay angle of the nucleon measured with respect to the normal to the production plane of K_S^0 and Σ^+ in the Σ^+ rest system.

P has been determined by fits to the polarization angular distribution for the decay mode $\Sigma^+ \rightarrow p\pi^0$ as a function of $\cos\Theta_K^{c.m.}$ for photon energies below and above 1.55 GeV. This decay mode is more sensitive than $\Sigma^+ \rightarrow n\pi^+$ due to the larger asymmetry parameter. The values of P are shown in fig. 12 and table 4 together with the previous measurement at SAPHIR [4]. The error bars refer to σ_w and σ_d respectively as described above.

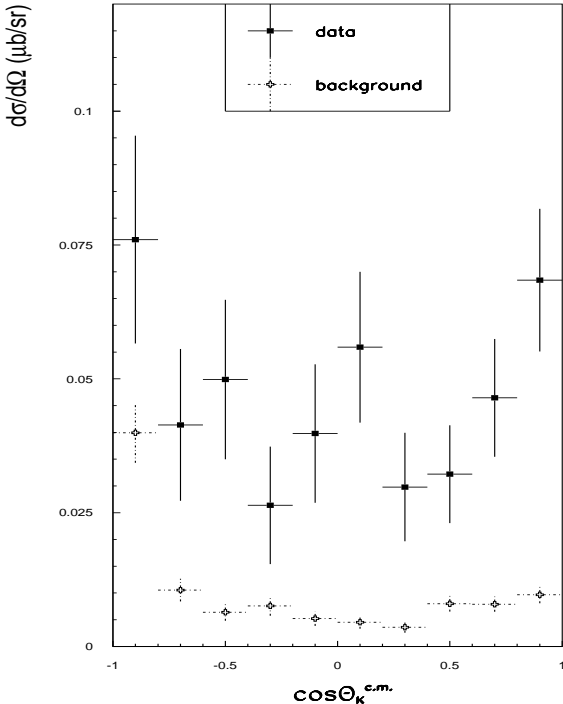


Fig. 9. Example of a measured differential cross section of $\gamma p \rightarrow K^0 \Sigma^+$ and the estimation of the total contribution of background from the reactions $p\pi^+\pi^-\pi^0$ and $n\pi^+\pi^+\pi^-$. Experimental data are shown in the photon energy range between 1.15 and 1.25 GeV for one data taking period (february 1998).

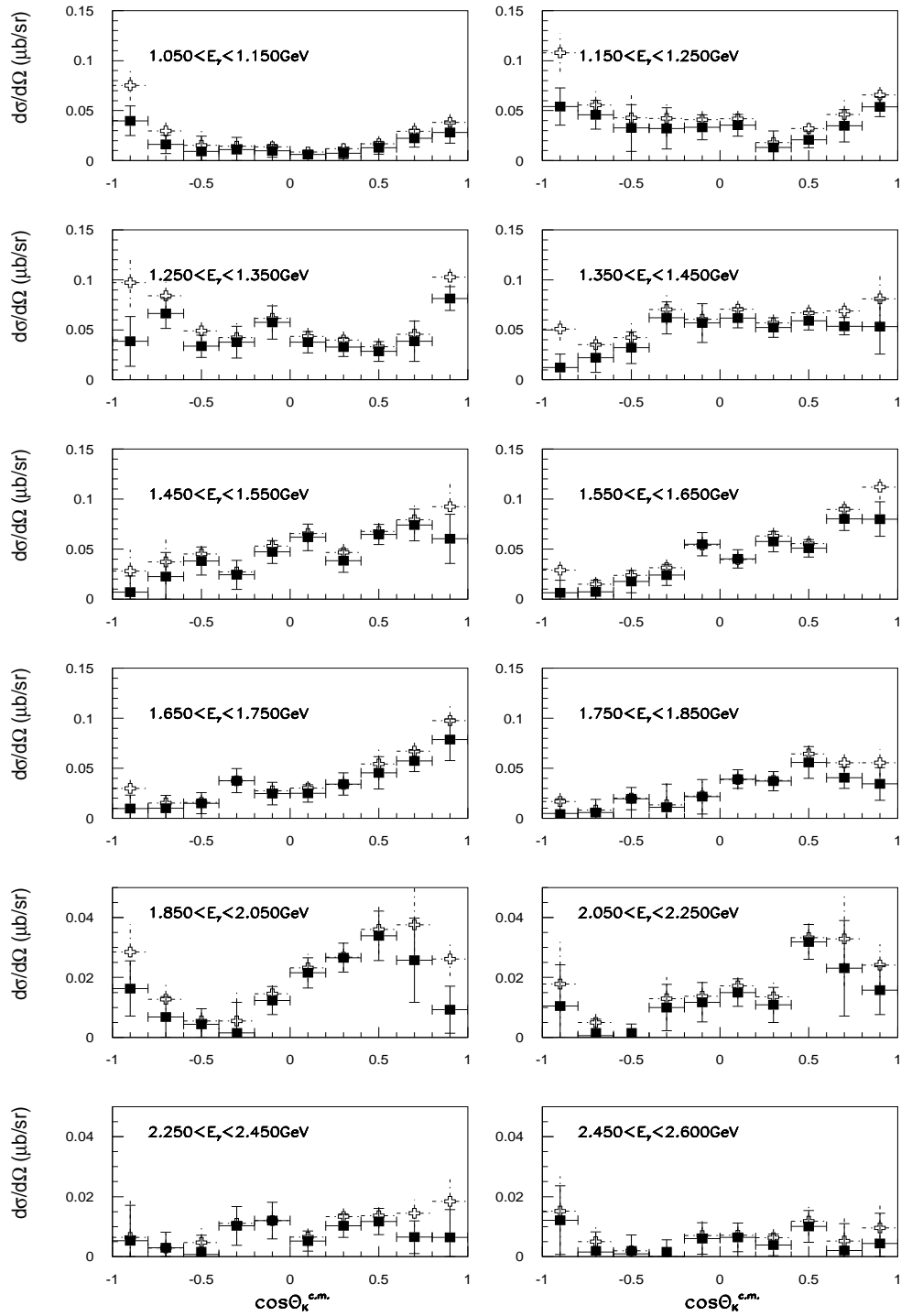


Fig. 10. Differential cross sections $\frac{d\sigma}{d\Omega}$ before (open crosses) and after (black squares) subtraction of background.

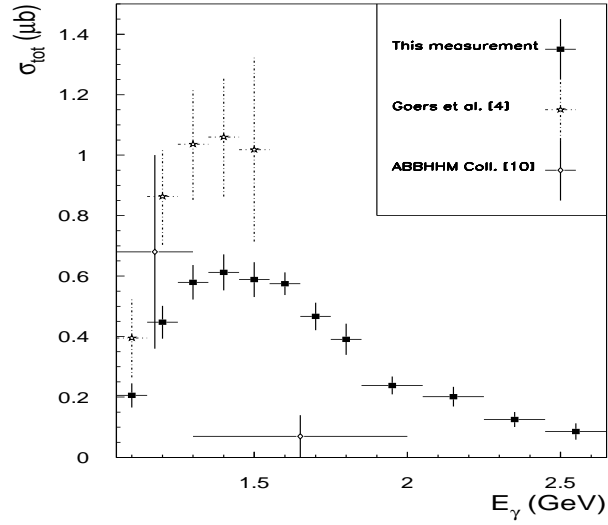


Fig. 11. Total cross section as a function of the photon energy after background subtraction in comparison with existing data.

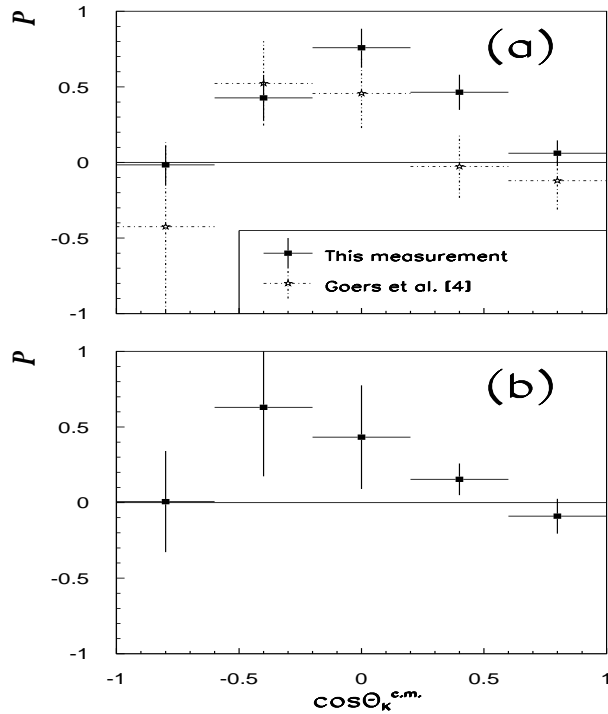


Fig. 12. Polarization parameter of Σ^+ in five bins of $\cos\theta_K^{c.m.}$ in the photon energy range (a) below 1.55 GeV and (b) above 1.55 GeV.

Table 2. Differential cross sections $d\sigma/d\Omega$ in μb in 12 bins of E_γ and 10 bins of $\cos \Theta_K^{c.m.}$, obtained after background subtraction.

$\cos \Theta_K^{c.m.}$	E_γ (GeV)			
	1.050 - 1.150	1.150 - 1.250	1.250 - 1.350	1.350 - 1.450
-1.0 - -0.8	0.040 ± 0.015	0.054 ± 0.019	0.038 ± 0.025	0.012 ± 0.013
-0.8 - -0.6	0.016 ± 0.009	0.046 ± 0.014	0.066 ± 0.015	0.022 ± 0.014
-0.6 - -0.4	0.009 ± 0.015	0.033 ± 0.023	0.034 ± 0.011	0.032 ± 0.016
-0.4 - -0.2	0.011 ± 0.012	0.032 ± 0.020	0.038 ± 0.016	0.062 ± 0.016
-0.2 - 0.0	0.010 ± 0.006	0.033 ± 0.013	0.057 ± 0.017	0.057 ± 0.020
0.0 - 0.2	0.006 ± 0.005	0.035 ± 0.011	0.038 ± 0.011	0.062 ± 0.010
0.2 - 0.4	0.007 ± 0.006	0.013 ± 0.016	0.033 ± 0.010	0.052 ± 0.010
0.4 - 0.6	0.013 ± 0.006	0.021 ± 0.008	0.028 ± 0.010	0.059 ± 0.009
0.6 - 0.8	0.022 ± 0.009	0.035 ± 0.016	0.039 ± 0.020	0.054 ± 0.009
0.8 - 1.0	0.028 ± 0.011	0.054 ± 0.010	0.081 ± 0.012	0.053 ± 0.027

$\cos \Theta_K^{c.m.}$	E_γ (GeV)			
	1.450 - 1.550	1.550 - 1.650	1.650 - 1.750	1.750 - 1.850
-1.0 - -0.8	0.007 ± 0.016	0.006 ± 0.013	0.010 ± 0.013	0.005 ± 0.015
-0.8 - -0.6	0.022 ± 0.024	0.007 ± 0.012	0.010 ± 0.013	0.006 ± 0.013
-0.6 - -0.4	0.038 ± 0.014	0.017 ± 0.011	0.015 ± 0.011	0.020 ± 0.011
-0.4 - -0.2	0.024 ± 0.015	0.024 ± 0.011	0.038 ± 0.012	0.011 ± 0.023
-0.2 - 0.0	0.047 ± 0.011	0.055 ± 0.012	0.025 ± 0.011	0.021 ± 0.017
0.0 - 0.2	0.062 ± 0.013	0.040 ± 0.009	0.025 ± 0.009	0.039 ± 0.009
0.2 - 0.4	0.038 ± 0.012	0.057 ± 0.010	0.034 ± 0.011	0.037 ± 0.010
0.4 - 0.6	0.065 ± 0.010	0.051 ± 0.009	0.045 ± 0.016	0.056 ± 0.016
0.6 - 0.8	0.074 ± 0.016	0.080 ± 0.012	0.057 ± 0.011	0.040 ± 0.011
0.8 - 1.0	0.060 ± 0.024	0.080 ± 0.017	0.079 ± 0.021	0.034 ± 0.016

$\cos \Theta_K^{c.m.}$	E_γ (GeV)			
	1.850 - 2.050	2.050 - 2.250	2.250 - 2.450	2.450 - 2.600
-1.0 - -0.8	0.016 ± 0.009	0.010 ± 0.014	0.005 ± 0.012	0.012 ± 0.011
-0.8 - -0.6	0.007 ± 0.007	0.001 ± 0.005	0.003 ± 0.005	0.002 ± 0.007
-0.6 - -0.4	0.004 ± 0.005	0.000 ± 0.005	0.001 ± 0.006	0.001 ± 0.006
-0.4 - -0.2	0.002 ± 0.010	0.010 ± 0.008	0.010 ± 0.007	0.000 ± 0.006
-0.2 - 0.0	0.012 ± 0.005	0.012 ± 0.007	0.012 ± 0.006	0.006 ± 0.005
0.0 - 0.2	0.022 ± 0.005	0.015 ± 0.005	0.005 ± 0.003	0.006 ± 0.005
0.2 - 0.4	0.027 ± 0.005	0.011 ± 0.006	0.010 ± 0.004	0.004 ± 0.004
0.4 - 0.6	0.034 ± 0.008	0.032 ± 0.006	0.012 ± 0.004	0.010 ± 0.005
0.6 - 0.8	0.026 ± 0.014	0.023 ± 0.016	0.007 ± 0.005	0.002 ± 0.009
0.8 - 1.0	0.009 ± 0.008	0.016 ± 0.008	0.006 ± 0.009	0.004 ± 0.010

Table 3. Total reaction cross sections in 12 bins of E_γ , obtained after background subtraction.

E_γ [GeV]	σ_{tot} (μb)
1.050 – 1.150	0.205 ± 0.040
1.150 – 1.250	0.447 ± 0.054
1.250 – 1.350	0.579 ± 0.057
1.350 – 1.450	0.612 ± 0.059
1.450 – 1.550	0.588 ± 0.058
1.550 – 1.650	0.575 ± 0.037
1.650 – 1.750	0.466 ± 0.045
1.750 – 1.850	0.391 ± 0.051
1.850 – 2.050	0.238 ± 0.029
2.050 – 2.250	0.201 ± 0.033
2.250 – 2.450	0.125 ± 0.025
2.450 – 2.600	0.086 ± 0.027

Table 4. Polarization parameter as a function of $\cos \Theta_K^{c.m.}$ in the photon energy range (a) up to 1.55 GeV and (b) above 1.55 GeV.

$\cos \Theta_K^{c.m.}$	$E_\gamma < 1.55$ GeV	$E_\gamma > 1.55$ GeV
-1.0 – -0.6	-0.016 ± 0.128	0.007 ± 0.334
-0.6 – -0.2	0.428 ± 0.152	0.630 ± 0.457
-0.2 – 0.2	0.759 ± 0.126	0.433 ± 0.343
0.2 – 0.6	0.464 ± 0.116	0.154 ± 0.105
0.6 – 1.0	0.061 ± 0.085	-0.090 ± 0.116

7 Comparison with $\gamma p \rightarrow K^+ \Sigma^0$

The reaction $\gamma p \rightarrow K^+ \Sigma^0$ was measured in the same experiment [3]. In the following the results are compared to $\gamma p \rightarrow K^0 \Sigma^+$.

Both reaction cross sections culminate at a photon energy around 1.45 GeV (see fig. 13). However, while $K^+ \Sigma^0$ shows a pronounced peak at this energy, $K^0 \Sigma^+$ varies more slowly and the cross section stays on a much lower level. If the cross sections in the peak region are dominated by the production of a Δ resonance (e.g. $S_{31}(1900)$ or $P_{31}(1910)$) Clebsch-Gordan coefficients predict that the ratio of cross sections is four in favor of $K^+ \Sigma^0$. The difference between both reactions is also evident in the angular dependence. As an example, the comparison of the $\frac{d\sigma}{d\Omega}$ distributions in the peak region is shown in fig. 14.

The polarizations of Σ^+ and Σ^0 are compared to each other in fig. 15. The Σ^0 polarization measured in bins of $\cos\theta_K^{c.m.}$ is found to rise as a function of the kaon production angle [3] while the Σ^+ polarization tends to go through a maximum value around $\cos\theta_K^{c.m.} \approx 0$. The Σ^0 polarization grows in magnitude when going from the lower to the higher energies. The Σ^+ polarization is consistent with little energy dependence.

An analysis of the data with respect to the underlying production mechanisms and resonance production can be made by the comparison to model calculations (see section 8).

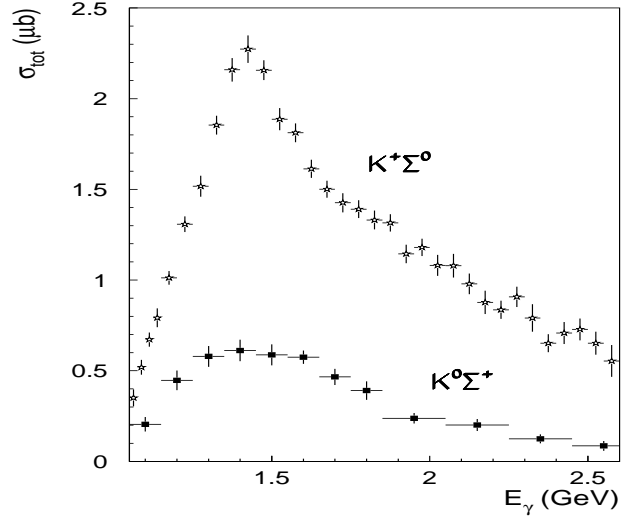


Fig. 13. Comparison of the total cross sections for $\gamma p \rightarrow K^0 \Sigma^+$ (black dots) and $\gamma p \rightarrow K^+ \Sigma^0$ (open stars).

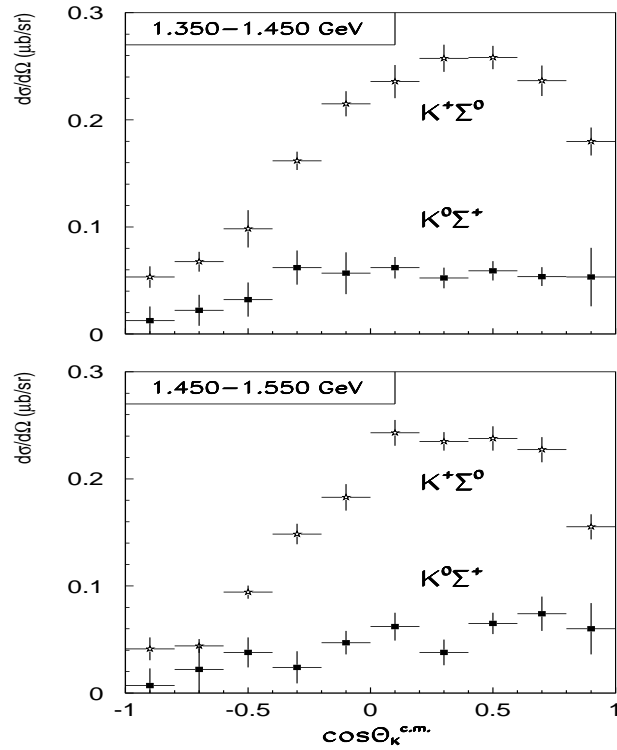


Fig. 14. Comparison of the differential cross sections for $\gamma p \rightarrow K^0 \Sigma^+$ (black squares) and $\gamma p \rightarrow K^+ \Sigma^0$ (open stars).

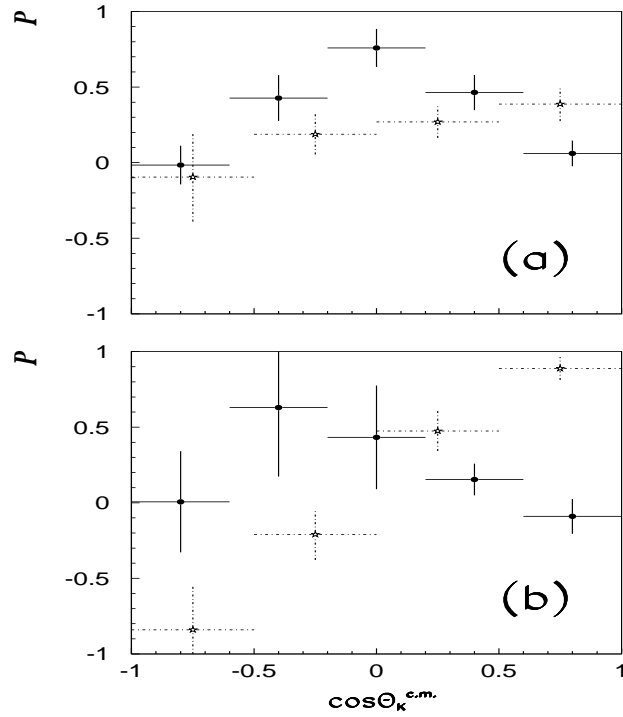


Fig. 15. Comparison of the polarization for $\gamma p \rightarrow K^0 \Sigma^+$ (black squares) and $\gamma p \rightarrow K^+ \Sigma^0$ (open stars) in the photon energy range (a) below 1.55 GeV and (b) above 1.55 GeV.

8 Comparison with theory

Here we discuss the comparison with model calculations of Bennhold and Mart [13] as well as with previous results from KAON-MAID [14]. Since the phenomenological KAON-MAID model² [13,14] was fitted to previous SAPHIR data [4,15], it obviously overpredicts the cross sections of this new measurement. This is clearly elucidated in Figs. 16 and 17. In order to see the effect of new data on the model, we refitted the corresponding coupling constants to the latest $K^+ \Sigma^0$ data [3] together with the $K^0 \Sigma^+$ data presented here using fixed values of the resonance parameters [12]. The result is shown in columns (b) of Table 5. For comparison, column (a) contains the result of the fit to the $K^+ \Sigma^0$ data only. It is obvious from Table 5 that the new data have a significant impact on the fit result. In general, including the new data reduces the coupling strengths of exchanged particles. This phenomenon can be understood from the fact that models which nicely fit the $K^+ \Sigma^0$ data tend to notoriously overpredict the $K^0 \Sigma^+$ cross sections [16]. All coupling constants need to be readjusted in order to reproduce the new $K^0 \Sigma^+$ data. Since both $g_{K\Lambda N}$ and $g_{K\Sigma N}$ coupling constants are fixed to the SU(3) values, the K^* coupling constants decrease by almost one order of magnitude. The tensor coupling of K_1 becomes also smaller after the inclusion of new data. It has been known that the K^* and K_1 exchanges strongly determine the shape of angular distribution of the differential cross sections. It is important to note that if the Born terms dominate the process then, due to the missing of K^0 intermediate state in the $K^0 \Sigma^+$ channel, the calculated differential cross sections show a backward peaking behavior. However, as shown by the hadronic form factor cut-off Λ_{Born} in Table 5, the model is not dominated by the Born terms. Therefore, only readjustment of the coupling constants is required in order to fit the new $K^0 \Sigma^+$ data. The K^* coupling constants, which are responsible for the divergent behavior of cross sections at higher energies [17], are strongly suppressed. Nevertheless, in view of the large χ^2/N_{dof} obtained after including the new data, further improvement is inevitably required.

Since there is no hint for a new resonance neither in the differential nor in the total cross section (see Figs. 16 and 17), an arbitrarily inclusion of new resonances to improve the χ^2 is by no means advocated. Instead, we left the masses and widths of N^* and Δ resonances as free parameters within certain ranges to be determined by the fit. The result is shown by Model 2 in Table 6, where we can see that the χ^2/N_{dof} is significantly reduced to 2.44. It is, however, especially interesting to see that both S_{11} and P_{13} masses are shifted to higher values (2167 MeV and 2133 MeV, respectively), whereas those of other resonance states are relatively stable. For P_{11} the fits prefer a width at the lowest value allowed. Reference [18] pointed

² The model consists of a background part which is constructed from the standard Born terms, K^* and K_1 t -channel exchanges, and the resonance part which includes the isospin 1/2 nucleon resonances $S_{11}(1650)$, $P_{11}(1710)$, and $P_{13}(1720)$, as well as the isospin 3/2 deltas $S_{31}(1900)$ and $P_{31}(1910)$.

Table 5. Coupling constants (g_i) and hadronic form factor cut-offs (Λ_i) extracted from fits without (a) and with (b) the new $K^0 \Sigma^+$ data. The Born coupling constants $g_{K\Lambda N}$ and $g_{K\Sigma N}$ are fixed to the SU(3) values.

Coupling Constants	(a)	(b)
$g_{K\Lambda N}/\sqrt{4\pi}$	-3.80	-3.80
$g_{K\Sigma N}/\sqrt{4\pi}$	1.20	1.20
$g_{K^*K\gamma} g_{K^*\Lambda N}^V/4\pi$	1.56	-0.22
$g_{K^*K\gamma} g_{K^*\Lambda N}^T/4\pi$	3.22	0.46
$g_{K_1K\gamma} g_{K_1\Lambda N}^V/4\pi$	-5.00	5.00
$g_{K_1K\gamma} g_{K_1\Lambda N}^T/4\pi$	-1.86	-0.57
$g_{N^*(1650)N\gamma} g_{K\Lambda N^*(1650)}/\sqrt{4\pi}$	-0.10	0.06
$g_{N^*(1710)N\gamma} g_{K\Lambda N^*(1710)}/\sqrt{4\pi}$	-0.25	0.04
$g_{\Delta(1900)N\gamma} g_{K\Sigma\Delta(1900)}/\sqrt{4\pi}$	0.11	0.04
$g_{\Delta(1910)N\gamma} g_{K\Sigma\Delta(1910)}/\sqrt{4\pi}$	0.46	0.58
$g_{N^*(1720)N\gamma} g_{K\Lambda N^*(1720)}/\sqrt{4\pi}^{(1)}$	-0.11	-0.01
$g_{N^*(1720)N\gamma} g_{K\Lambda N^*(1720)}/\sqrt{4\pi}^{(2)}$	0.34	-0.71
$g_{K_1^0 K^0 \gamma} / g_{K_1^+ K^+ \gamma}$	-	-0.12
Λ_{Born} (GeV)	0.53	0.55
$\Lambda_{\text{Res.}}$ (GeV)	1.38	1.07
χ^2/N_{dof}	2.36	4.14
N_{data}	676	818

Table 6. Extracted masses (M) and widths (Γ) of resonances (in MeV) from different models. Model 1 and Model 2 are described in the paper. Both $K^+ \Sigma^0$ and $K^0 \Sigma^+$ data are used in this fit.

Resonance	Mass or Width	Original value [12]	Model 2	Model 1
$S_{11}(1650)$	M	1650	2167	1795
	Γ	150	186	158
	M	-	-	2112
	Γ	-	-	400
$P_{11}(1710)$	M	1710	1690	1680
	Γ	100	100	100
$P_{13}(1720)$	M	1720	2133	2141
	Γ	150	256	279
$S_{31}(1900)$	M	1900	1920	1900
	Γ	200	355	329
$P_{31}(1910)$	M	1910	1936	1800
	Γ	250	399	400
χ^2/N_{dof}		4.14	2.44	1.76

out that such a behavior could be an indication for the existence of another resonance with a relatively different mass. As a first step to check this conjecture, we put two S_{11} resonances and leave their masses and widths to be determined by the fit. As shown by Model 1 in the same Table, we obtain from such a fit two S_{11} signals with masses 1795 MeV and 2112 MeV, respectively, which seemingly supports the finding in Ref. [18]. This could be another indication that more “missing resonances” are required

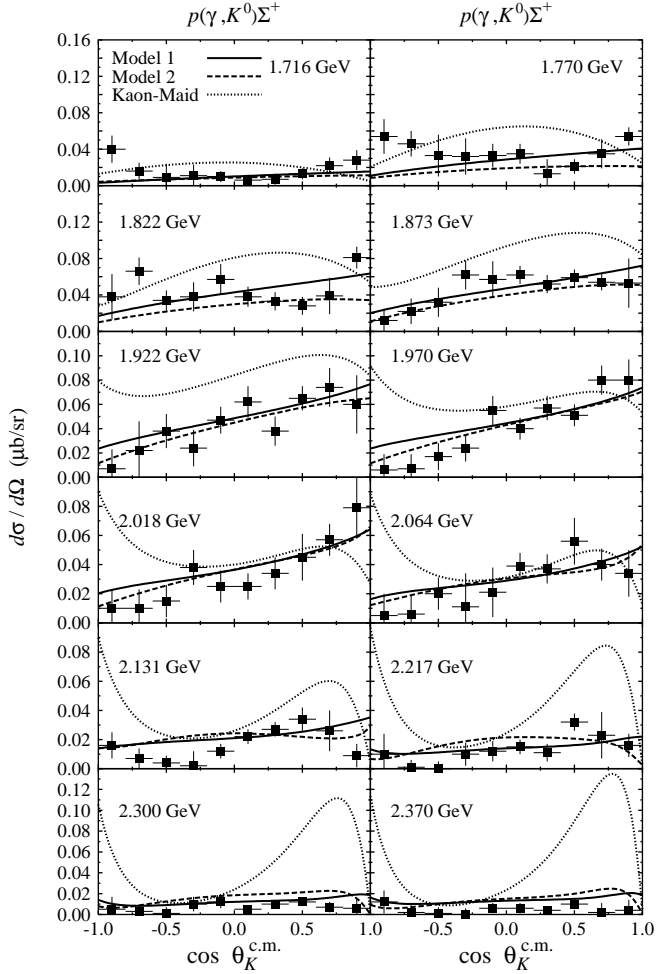


Fig. 16. Differential cross sections for $K^0 \Sigma^+$ photoproduction. Dotted lines are prediction from the KAON-MAID model [14], dashed lines are obtained from Model 2, whereas solid lines exhibit the prediction of Model 1. The c.m. energy W is shown in each panel.

to explain kaon photoproduction process, a point which should be addressed in future studies.

Figure 16 compares the differential cross sections obtained from different isobar models. It is evident from this figure that the KAON-MAID fit to the previous data is unable to reproduce neither the shape nor the magnitude of differential cross sections. In contrast to this, both Model 1 and Model 2 can fairly describe these new data up to some structures shown, except at low energies for backward angles. At forward directions Model 1 tends to produce more forward peaking cross sections at high energies than Model 2. The fact that Model 2 cannot reproduce total cross section data at energies below 1900 MeV (Fig. 17) is due to the lack of resonances with $M \approx 1800$ MeV (see Table 6). In Model 1 the fitted mass of the first S_{11} and that of the P_{31} are in this region. We also note that in the case of the KAON-MAID fit on the previous data the divergent behavior of the total cross section at high energies is attributed to the large value of the Λ_{Born} cut-off (0.82 GeV). At this region a slight increment in total cross

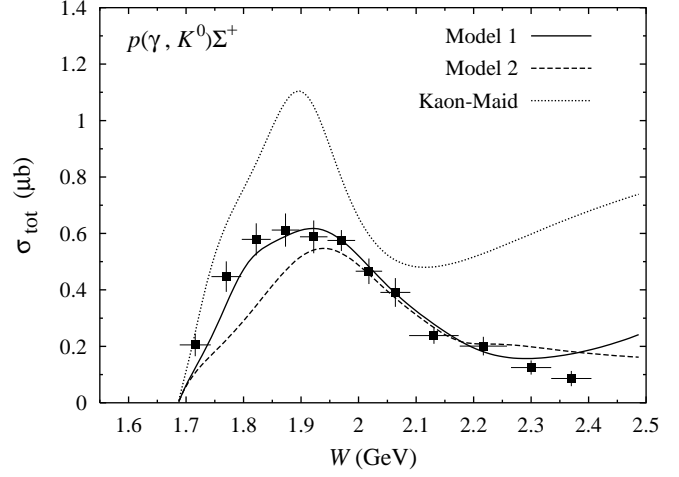


Fig. 17. As in Fig. 16, but for the total cross section.

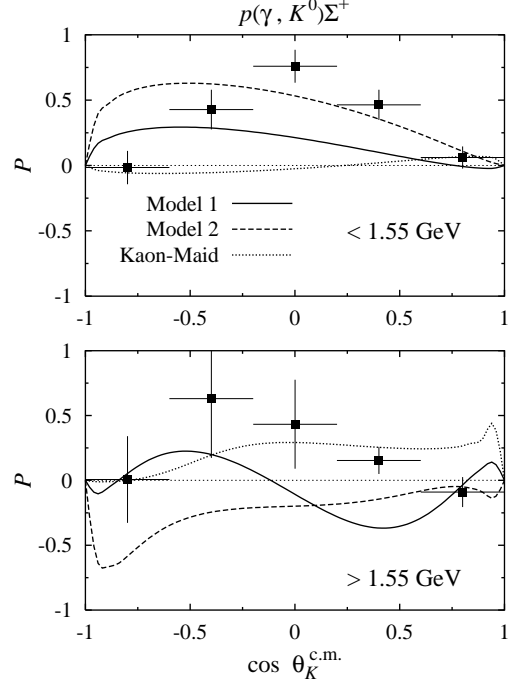


Fig. 18. As in Fig. 16, but for the Σ^0 recoil polarization.

section is also observed in Model 1, but not in Model 2. Figure 18 shows that neither model can reproduce the Σ^+ recoil polarization data which tend to peak at $\theta_K^{c.m.} \approx 90$ degrees. From the fit point of view this can be understood since the number of data is too scarce to compete with the cross sections one and the energy bins of the data are too broad to compare with a single energy prediction. On the other side, this result shows that polarization data are still powerful to severely constrain the proliferating of the models, provided that the corresponding accuracy can be significantly improved.

9 Summary

A new measurement of the reaction $\gamma p \rightarrow K^0 \Sigma^+$ carried out with the SAPHIR detector at ELSA is reported. The results comprise measurements of cross section and hyperon polarization as a function of kaon production angle and photon energy in the photon energy range from the reaction threshold up to 2.6 GeV. The reaction cross section integrated over the angular range grows up to a photon energy around ≈ 1.4 GeV and falls monotonously from there up to the highest measured energy. The reaction cross section is below that of $\gamma p \rightarrow K^+ \Sigma^0$ and varies less with photon energy and kaon production angle. The Σ^+ is polarized mainly in the angular region of $\cos \theta_K^c \approx 0$. The data can be fairly well described within the framework of isobar model calculations.

We would like to thank the technical staff of the ELSA machine group for their invaluable contributions to the experiment. We gratefully acknowledge the support by the Deutsche Forschungsgemeinschaft in the framework of the Schwerpunktprogramm "Investigation of the hadronic structure of nucleons and nuclei with electromagnetic probes" (SPP 1034 KL 980/2-3).

References

1. S. Capstick and W. Roberts, Phys. Rev. D 58, 074011 (1998)
2. U. Löring, K. Kretzschmar, B. Ch. Metsch, H.-R. Petry, Eur. Phys. J. A 10, 309 (2001); U. Löring, B. Ch. Metsch and H.-R. Petry, Eur. Phys. J. A 10, 395 (2001) and Eur. Phys. J. A 10, 447 (2001); B. Ch. Metsch, U. Löring, D. Marten and H.R. Petry, Eur. Phys. J. A 18, 189 (2003).
3. K.-H. Glander et al., The SAPHIR Collaboration, Eur. Phys. J. A 19, 251 (2004).
4. S. Goers et al., The SAPHIR Collaboration, Phys. Lett. B 464, 331 (1999).
5. W. J. Schwille et al., The SAPHIR Collaboration, Nucl. Instr. Meth. A 344, 470 (1994).
6. D. Husmann, W. J. Schwille, Phys. Bl. 44, 40 (1988).
7. R. Burgwinkel, doctoral thesis, Bonn university (1996), Bonn-IR-9602; J. Barth, doctoral thesis, Bonn University (2002), Bonn-IR-02-6.
8. K.-H. Glander, doctoral thesis, Bonn university (2003), Bonn-IR-2003-05, <http://saphir.physik.uni-bonn.de/saphir/thesis.html>.
9. R. Lawall: Messung der Reaktion $\gamma p \rightarrow K^0 \Sigma^+$ für Photonenergien bis 2.65 GeV mit dem SAPHIR-Detektor an ELSA, doctoral thesis, Bonn University, BONN-IR-2004-01, <http://saphir.physik.uni-bonn.de/saphir/thesis.html>.
10. Aachen-Berlin-Bonn-Hamburg-Heidelberg-München Collaboration, Physical Review 188, 2060 (1969).
11. T. D. Lee, J. Steinberger, G. Feinberg, P. K. Kabir, C. N. Yang, Phys. Rev. 106, 1367 (1957); R. Gatto, Phys. Rev. 109, 610 (1958).
12. Review of Particle Physics (S. Eidelman et al.), Phys. Lett. B 592, 1 (2004).
13. C. Bennhold, T. Mart et al., preprint nucl-th/9901066; C. Bennhold, H. Haberzettl, T. Mart in Proc. of the second international conference on perspectives in hadronics physics, World Scientific, Singapore (1999); T. Mart, C. Bennhold, Phys. Rev. C 61 (12), 012201 (2000); C. Bennhold et al., preprint nucl-th/0008024.
14. KAON-MAID: <http://www.kph.uni-mainz.de/MAID/kaon/kaonmaid.html>.
15. M. Q. Tran et al., The SAPHIR Collaboration, Phys. Lett. B 445, 20 (1998).
16. T. Mart, C. Bennhold and C. E. Hyde-Wright, Phys. Rev. C 51, 1074 (1995).
17. T. Mart, S. Sumowidagdo, C. Bennhold and H. Haberzettl, preprint nucl-th/0002036.
18. T. Mart, A. Sulaksono and C. Bennhold, in *Proceedings of the International Symposium on Electrophotoproduction of Strangeness on Nucleons and Nuclei (SENDAI 03)*, Sendai, Japan, 16-18 Jun 2003, edited by K. Maeda, H. Tamura, S.N. Nakamura, O. Hashimoto (World Scientific, Singapore, 2004) p.65; preprint nucl-th/0411035.